Journal of Materials Chemistry C

PAPER

View Article Online
View Journal | View Issue



Cite this: J. Mater. Chem. C, 2016, 4, 286

# Tailoring the microstructure and charge transport in conjugated polymers by alkyl side-chain engineering†

Sadiara Fall,[a] Laure Biniek,[b] Yaroslav Odarchenko,[c] Denis V. Anokhin,[de] Grégoire de Tournadre,[f] Patrick Lévêque,[a] Nicolas Leclerc,[g] Dimitri A. Ivanov,*[cd] Olivier Simonetti,[f] Louis Giraudet[f] and Thomas Heiser*[a]

Charge transport in conjugated polymers is critical to most optoelectronic devices and depends strongly on the polymer structure and conformation in the solid state. Understanding the correlations between charge carrier mobility, energy disorder and molecular assembly is therefore essential to improve device performances. Alkyl side-chains contribute to intermolecular interactions and are key to controlling the polymer microstructure and electronic properties. Investigating a set of polymers with common conjugated units but different side-chain functionalization provides new insights into the complex structure–transport relationship. Here, field-effect transistors and space-charge-limited current devices are used together with *in situ* grazing-incidence wide-angle X-ray scattering to study charge transport and morphology in a series of donor–acceptor copolymers. Probing hole mobility as a function of carrier density and orientation permits us to assess energy disorder and hopping rate anisotropy, while X-ray diffraction allows us to link transport properties to the polymer microstructure. We show that branched side-chains enhance structural and energy disorder and lead to isotropic transport, whereas linear chains induce either a common lamellar structure or a more exceptional pseudo-hexagonal columnar phase with a helicoidal polymer conformation. The latter enhances out-of-plane mobility but increases energy disorder possibly due to larger interring torsion angles.

Received 19th September 2015,
Accepted 22nd November 2015

DOI: 10.1039/c5tc03000e

www.rsc.org/MaterialsC



## 1. Introduction

Charge transport in semiconducting polymers is a key factor for the operation of most organic optoelectronic devices and has attracted a lot of attention from the scientific community over the last few decades. Although significant progress has been achieved in the design of polymers exhibiting relatively high charge carrier mobilities, the multifaceted relationship between the polymer molecular structure and the charge transport properties remains a challenging field of investigation.[1–4]

The complex link between molecular structure and transport originates from the fact that subtle variations in intra-molecular charge delocalization and inter-molecular coupling strength can have a strong impact on charge carrier hopping rates. Both intermolecular and intramolecular hopping depend in a non-trivial way on molecular planarity, chain length, chain folding, molecular packing, as well as on the nature and grafting position of alkyl side-chains. For instance, as shown by Vukmirović using atomistic multiscale modelling, the electronic density of states (DOS), which underlies charge transport, is expected to broaden with conjugated backbone shape irregularities and interring torsions introduced by alkyl side-chains.[5] On the other hand, however, side-chains are also predicted to weaken fluctuations in the electrostatic coupling strength, thereby reducing energy disorder. Sirringhaus *et al.* recently confirmed the strong impact of side-chains on energy disorder for a range of state-of-the-art copolymers, and provided guidelines for the design of low disorder conjugated polymers.[6] However, the structure–transport relationships are far from being fully understood.

Since a predictive model for charge carrier mobilities in new conjugated polymers is not available, methodical experimental investigations of both electrical and morphological properties remain crucially important.[3] Charge transport can be strongly

[a] Laboratoire ICube, DESSP, Université de Strasbourg, CNRS, 23, rue de Loess, 67037 Strasbourg, France. E-mail: thomas.heiser@unistra.fr
[b] ICS, Université de Strasbourg, 23 rue de Loess, 67034 Strasbourg, France
[c] Institut des Sciences des Matériaux de Mulhouse, CNRS UMR 7361, 15 rue Jean Starcky, B.P. 2488, 68057 Mulhouse Cedex, France. E-mail: dimitri.ivanov.2014@gmail.com
[d] lomonosov Moscow State University, Faculty of Fundamental Physical and Chemical Engineering, GSP-1, 1-51 Leninskie Gory, Moscow, 119991, Russia
[e] IPCP RAS, Semenov Prospect 1, Chernogolovka, 141432, Russia
[f] Laboratoire de Recherche en Nanosciences, Université Reims Champagne Ardenne, Moulin de la Housse, 51687 Reims, France
[g] ICPEES, Université de Strasbourg, Ecole Européenne de Chimie, Polymères et Matériaux, 25 rue Becquerel, 67087 Strasbourg, France

† Electronic supplementary information (ESI) available. See DOI: 10.1039/c5tc03000e

anisotropic and dependent on charge carrier densities as well as on electric field strength. A profound understanding can therefore only be reached by probing charge transport along various orientations and in distinct electronic environments. The combined use of organic field-effect transistors (OFET) and space-charge-limited-current (SCLC) single carrier devices is a convenient way to approach this goal.[7,8] Not only do both devices explore in-plane and out-of-plane (*i.e.* parallel or perpendicular to the device substrate) transport respectively, but their operation allows us furthermore to cover a large span of charge carrier densities and electric field intensities. This methodology has been used successfully before to investigate charge transport in poly(*p*-phenylene vinylene) and polythiophene derivatives.[9] An eventual limitation of this approach lies in the possibility that the polymer microstructure may differ in both devices due to different substrates. This risk can however be minimized by combining charge transport measurements with *in situ* microstructure characterization.

In this work, we present an in-depth study of charge transport and thin-film microstructure of a series of conjugated low band-gap polymers which have been developed previously and used as electron-donors in bulk heterojunction solar cells.[10,11] The polymers are composed of alternating electron-deficient benzo[2,1,3]thiadiazole (Bz) and electron-rich thiophene (Th) and thieno[2,3-*b*]thiophene (TT) units and differ essentially in the nature of their solubilizing side chains and in the number of thiophene units. The latter parameter controls the side-chain density along the polymer backbone since only thiophene units carry side-chains. While our previous investigations showed that these structural changes had a considerable impact on the material photovoltaic properties,[10,11] we will focus herein on their influence on charge transport and thin film microstructure. Following the approach outlined above, we used OFET and SCLC devices to study the hole mobility, together with *in situ* GIWAXS experiments to characterize the thin film morphology. We show that minor modifications of the molecular structure can profoundly alter the microstructure and strongly impact transport anisotropy and energy disorder. In particular, branched side chains tend to enhance both structural and energy disorder, leading to a rather low isotropic hole mobility, while linear chains give rise to more ordered structures and strongly anisotropic transport. We further show that upon decreasing the side-chain grafting density along the polymer backbone the polymer assembly switches from a lamellar structure to an unusual helicoidal conformation, inducing an order of-magnitude change in the in-plane and out-of-plane hole mobilities. Interestingly, the out-of plane mobility, which is crucial to the operation of vertical devices such as organic solar cells, is enhanced by the helicoidal conformation.

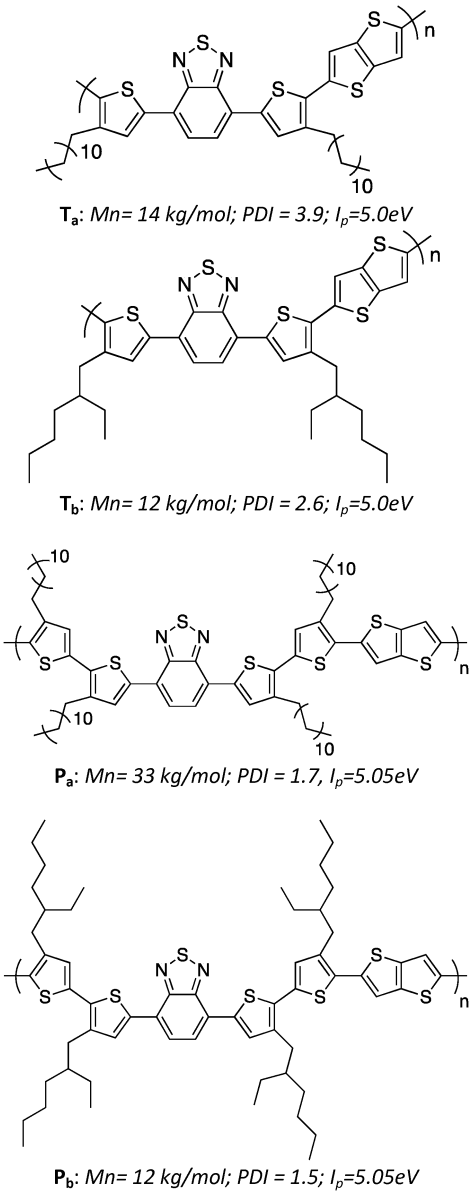


Fig. 1 Molecular structure and relevant properties of the investigated polymers.

## 2. Results

### 2.1 Materials

The molecular structures and relevant properties of the investigated polymers are summarized in Fig. 1. The synthesis procedures, as well as detailed molecular characterizations, have been published before.[10] Shortly, the number of Th units per monomer was either 2 (for $\mathbf{T_a}$, $\mathbf{T_b}$) or 4 (for $\mathbf{P_a}$, $\mathbf{P_b}$). Linear dodecyl side chains were grafted on the Th units for $\mathbf{T_a}$ and $\mathbf{P_a}$, while branched ethyl–hexyl chains were used for $\mathbf{T_b}$ and $\mathbf{P_b}$. The molecular weights and ionization potentials, $I_p$, are within the same range for all four polymers, while the polydispersity index is slightly lower for $\mathbf{P_a}$ and $\mathbf{P_b}$.

### 2.2 Charge transport

**SCLC devices.** The current–voltage characteristics of the SCLC devices are shown in Fig. 2. To facilitate the comparison between devices with different polymer layer thicknesses, we plotted $J \times L^3$ *versus* $V$, where $J$ represents the current density,

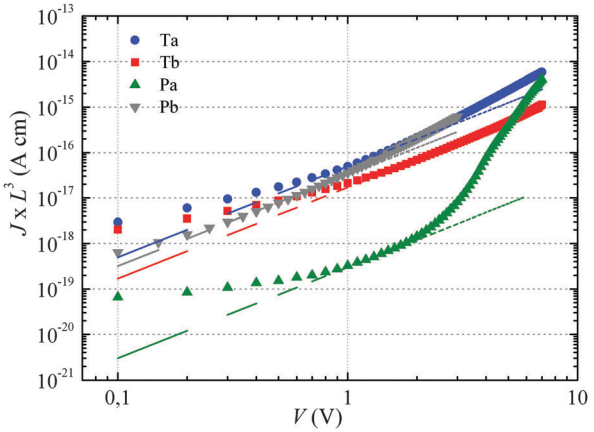


Fig. 2 Space-charge-limited current on as-cast polymers. For $\mathbf{P_a}$ the curve has been obtained by averaging the current–voltage data of four devices processed under identical conditions. The dashed lines correspond to a fit in the voltage range where $J$ follows a square-law dependence (constant mobility) on the voltage.

$V$ the applied voltage and $L$ the polymer layer thickness. For each polymer, supplementary curves obtained on other film thicknesses are given in the ESI.†

If the current is space-charge-limited, the experimental curves should follow the conventional Mott–Gurney law,[12]

$$J \times L^3 = \frac{9}{8}\varepsilon_r \varepsilon_0 \mu_\perp V^2 \quad (1)$$

where $\varepsilon_0$ is the permittivity of free space, $\varepsilon_r$ the polymer dielectric constant (taken as 3, similar to poly(3-hexylthiophene)),[13] and $\mu_\perp$ the possibly voltage dependent out-of-plane mobility. As the polymer ionization potentials (Fig. 1) are close to the PEDOT:PSS work-function (~5.1 eV), all polymer/PEDOT:PSS interfaces should exhibit a low injection barrier and eqn (1) should apply. This has indeed been found to hold for $\mathbf{T_a}$, $\mathbf{T_b}$ and $\mathbf{P_b}$, as evidenced by the thickness dependence of the current–voltage curves (see ESI†). $\mathbf{P_a}$ however behaves differently. First, the current–voltage characteristics showed significant sample-to-sample fluctuations (individual curves are shown in the ESI†). Also, the deviation from the thickness scaling predicted by eqn (1) was above the noise level, suggesting the existence of a non-negligible injection barrier. To allow nevertheless a comparison with the other polymers, we plotted in Fig. 2 the average current–voltage curve obtained on different devices.

The dashed lines in Fig. 2 have been obtained by fitting eqn (1) to the experimental curves in a voltage range where $J$ follows a square-law dependence (constant mobility). This voltage range is limited at low values by Ohmic currents induced by either dark conductivity (unintentional doping) or carrier diffusion at the metal/semiconductor interface,[13–15] while at high voltages, field-dependent[16] and/or charge-carrier-density dependent charge transport may lead to a more pronounced current increase.[9,17] For $\mathbf{T_a}$, $\mathbf{T_b}$ and $\mathbf{P_b}$ the current follows the expected $V^2$ law over a reasonable voltage range and can therefore be used to estimate the low-field out-of-plane mobility. This is not the case for $\mathbf{P_a}$ for which the presumable injection barrier allows only an estimate for the lower limit of mobility. The $\mu_\perp$ values are summarized in Table 1 and are of the same order of magnitude for $\mathbf{T_a}$, $\mathbf{T_b}$ and $\mathbf{P_b}$, while the estimate for the $\mathbf{P_a}$ mobility is two orders of magnitude lower. These results will be further discussed below.

**Organic field effect transistors.** The OFET transfer characteristics in the linear regime are represented in Fig. 3 The transistor output characteristics are given in the ESI.† At high gate voltages, the current increases almost linearly with $V_g$ (dashed lines in Fig. 3a). The in-plane field-effect mobility ($\mu_\parallel$) values extracted within this voltage range using the standard transistor model equation

$$\mu_\parallel(V_g) = \frac{L_c}{W V_{ds} C_{ox}} \left.\frac{\partial I_{ds}}{\partial V_g}\right|_{V_{ds}} \quad (2)$$

are summarized in Table 1. $I_{ds}$ represents the drain current, $V_{ds}$ the drain voltage, $C_{ox}$ the dielectric capacitance (15 nF cm$^{-2}$) and $V_g$ the gate voltage.[18]

For $\mathbf{T_b}$ and $\mathbf{P_b}$, the $\mu_\parallel$ values are comparable ($\sim 5 \times 10^{-4}$ cm$^2$ V$^{-1}$ s$^{-1}$) and exceed $\mu_\perp$ by roughly one order of magnitude. On the other hand a significantly higher $\mu_\parallel$ value ($\sim 10^{-3}$ cm$^2$ V$^{-1}$ s$^{-1}$) is found for $\mathbf{P_a}$, about three orders of magnitude above the lower estimate of $\mu_\perp$. Surprisingly, the in-plane mobility of $\mathbf{T_a}$ ($\sim 3 \times 10^{-5}$ cm$^2$ V$^{-1}$ s$^{-1}$) is about a factor of four lower than the corresponding out-of-plane mobility.

The strong contrast between the OFET and SCLC results can be partly explained by taking into account the influence of the charge carrier density ($p$) set by the gate voltage.[19] Normalizing the drain current by the mobility given in Table 1 (Fig. 3b) highlights distinctive gate-voltage dependences. For $\mathbf{P_a}$ the drain current decreases almost linearly down to the threshold voltage, while for $\mathbf{T_a}$, $\mathbf{T_b}$ and $\mathbf{P_b}$, a significant positive curvature occurs at low $V_g$. As no contact resistance effects are seen neither in the OFET output characteristics (see ESI†) nor in the transfer characteristics at high gate voltages, it is likely that the non-linear transfer characteristics at low $V_g$ are due to a charge carrier density dependent mobility. As $\mu_\parallel$ is proportional to the slope of $I_d$ ($V_g$), the mobility is seen to increase with the gate voltage for $\mathbf{T_a}$, $\mathbf{T_b}$, and $\mathbf{P_b}$, while it remains almost constant for $\mathbf{P_a}$. To go a step

Table 1 Mobility values extracted from SCLC ($\mu_\perp$) and OFET ($\mu_\parallel$) devices. $E_0$ describes the width of the exponential DOS, as extracted from temperature dependent field-effect mobility measurements. The mobility error margins correspond to the standard deviation of the measurements performed on at least three devices. The $E_0$ error margins are equal to the standard error of the linear fit of the temperature dependent $k$ exponent (see Fig. S5, ESI)

| Polymer | $\mathbf{T_a}$ | $\mathbf{T_b}$ | $\mathbf{P_a}$ | $\mathbf{P_b}$ |
|---|---|---|---|---|
| $\mu_\perp$ (cm$^2$ V$^{-1}$ s$^{-1}$) | $(1.3 \pm 0.5) \times 10^{-4}$ | $(4.7 \pm 1.0) \times 10^{-5}$ | $>10^{-6}$ | $(8.5 \pm 2.0) \times 10^{-5}$ |
| $\mu_\parallel$ (cm$^2$ V$^{-1}$ s$^{-1}$) | $(3.1 \pm 0.3) \times 10^{-5}$ | $(5.5 \pm 0.2) \times 10^{-4}$ | $(1.3 \pm 0.3) \times 10^{-3}$ | $(5.5 \pm 0.5) \times 10^{-4}$ |
| $E_0$ (meV) | $32 \pm 2$ | $35 \pm 1.5$ | $28 \pm 1$ | $34 \pm 1$ |

 

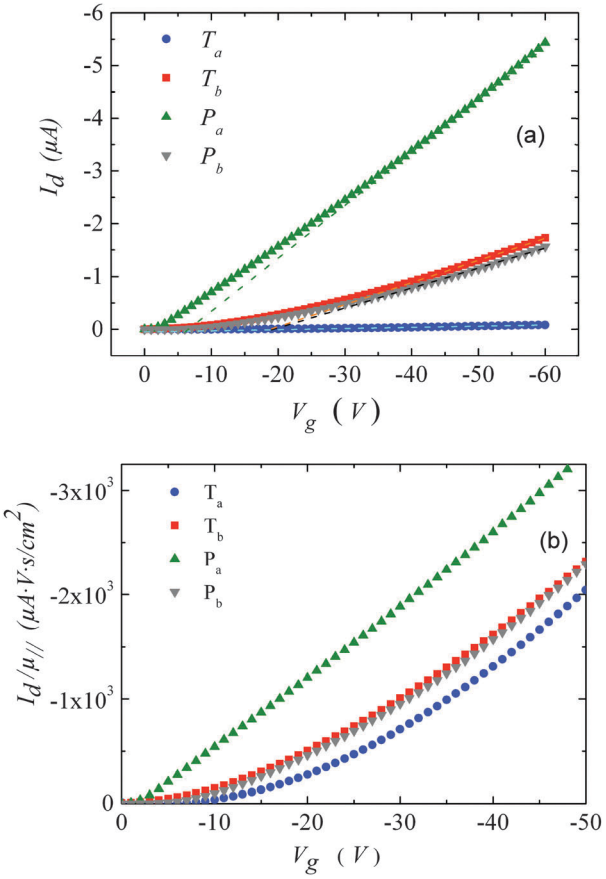


Fig. 3 (a) Transfer characteristics measured at room temperature. (b) Drain current, normalized by the mobility values given in Table 1 *versus* gate-voltage. The drain voltage was set to −10 V.

further in the comparison between SCLC and OFET results, we need to quantify $p$ in both experiments. In SCLC devices, the charge carrier density is non-uniform over the semiconductor layer thickness and depends on the applied voltage and film thickness. An average value of $p$ can nevertheless be obtained from the standard drift model of space-charge-limited transport,[12,17] given by

$$p = \frac{3}{2}\left(\frac{\varepsilon_0 \varepsilon_s V}{eL^2}\right) \quad (3)$$

Note that eqn (3) neglects the contribution of charge carrier diffusion at the ohmic contacts.[14] The latter is expected to be low for the film thicknesses used in this study. In the transistor channel, $p$ is known to decrease rapidly along the out-of plane direction, confining the drain current to a few nanometer thin layer.[20] As a consequence, the field-effect mobility extracted from eqn (2) is, strictly speaking, a result of transport in the presence of a non-uniform carrier density. However, according to the percolation model developed by Vissenberg *et al.*[21] for an exponential DOS, eqn (2) leads to a mobility value, which would be observed in the presence of an effective uniform charge carrier density given by

$$p = \left[\frac{\left(C_{ox}\left(V_g - V_T\right)\right)^2}{2E_0\varepsilon_0\varepsilon_r}\right] \quad (4)$$

where $V_T$ is the threshold voltage and $E_0$ the width of the density of state distribution [DOS($E$) $\propto$ exp($-E/E_0$)].[7] The relevance of describing the energetic landscape in conjugated polymers by an exponential rather than a Gaussian DOS may be questionable and is still under debate in the literature.[22,23] Still, Tanase *et al.* showed that for poly(*p*-phenylene vinylene) derivatives, the exponential DOS obtained using Vissenberg's model follows closely the Gaussian DOS within the finite energy interval spanned by the Fermi-level during the field-effect measurements.[7] It is likely that the same holds true for other disordered organic semiconductors. Here, we use eqn (4) to estimate the effective charge carrier density at each gate voltage and apply the results to rescale $\mu(V_g)$ into $\mu(p)$. The $E_0$ values that are needed to perform this operation have been extracted from temperature dependent current–voltage measurements (see ESI†) and are summarized in Table 1. The values obtained for **$T_a$**, **$T_b$** and **$P_b$** are in the same range than those reported previously for other conjugated polymers, such as P3HT (36 meV)[8] or poly(p-phenylene vinylene) (PPV) derivatives (from 28 to 46 meV).[7,23] The low value found for **$P_a$** (28 meV) points towards a highly ordered structure. We note however that Vissenberg's model may in this case underestimate $E_0$, due to a strong transport anisotropy (see below).

Using both, the $E_0$ estimates and eqn (3), we plotted the SCLC and OFET mobility values as a function of charge carrier density on the same graph (Fig. 4). The solid lines represent field-effect mobilities extrapolated to low charge carrier densities. The dashed lines represent the upper and lower limits for $\mu_{||}$ taking into account the error margin on $E_0$. Several conclusions can be drawn from Fig. 4. For the branched side-chain polymers

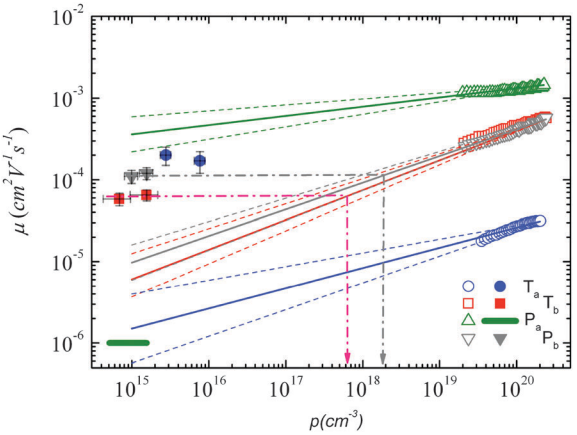


Fig. 4 Mobility as a function of the charge carrier density as measured in OFET (open symbols) and SCLC devices (full symbols) at room temperature. For SCLC measurements, eqn (3) was used to estimate $p$ for an applied voltage of 1 V and two different film thicknesses. The green horizontal line indicates the lower limit of the SCLC mobility for **$P_a$**. The solid and dashed lines represent extrapolations of the field-effect mobility measured at a carrier concentration $p_h$, corresponding to −60 V gate voltage (Table 1), down to a low carrier concentration $p_l$, following $\mu(p_l) = \mu(p_h) \times (p_l/p_h)^{\frac{E_0}{kT}-1}$.[21] For $E_0$, the average values given in Table 1 (solid lines) as well as the upper and lower limits (dashed lines) have been used. The dash-dotted lines indicate the carrier concentration below which the hole mobilities in either **$P_b$** (grey line) or **$T_b$** (red line) are expected to remain constant.

$\mathbf{T_b}$ and $\mathbf{P_b}$, the SCLC mobilities are significantly higher than the extrapolated field-effect values. This suggests the existence of a transition from a carrier density dependent to a constant mobility at a critical carrier density $p_c$ (indicated by an arrow in Fig. 4). According to the Gaussian disorder model (GDM), such a transition is expected to occur at a hole density given by[24]

$$p_c = N \times \exp\left[-\frac{1}{2}\left(\frac{\sigma}{kT}\right)^2\right] \quad (5)$$

where $N$ is the density of hopping sites and $\sigma$ the width of the Gaussian distribution. Taking $N = 10^{21}$ cm$^{-3}$ (which is a rough estimate of the number of polymer repeat units per cm$^3$),[23] and the $p_c$ values indicated in Fig. 4 (arrows), we obtain a Gaussian width of $\sigma = 95 \pm 5$ meV for $\mathbf{T_b}$ and $\mathbf{P_b}$, which is close to values reported previously for other disordered organic semiconductors (typically around 100 meV).[25] We may thus conclude that for both polymers the energetic disorder is sufficient to explain the discrepancy between SCLC and OFET mobilities, revealing highly disordered materials with isotropic transport. We further note that in our SCLC experiments, the charge carrier density given by eqn (3) is more than one order of magnitude below $p_c$, suggesting that the deviation from eqn (1) at high voltage (see Fig. 2) is a signature of an electric-field dependent rather than a charge-carrier-density dependent mobility.

The situation is significantly different for $\mathbf{P_a}$ and $\mathbf{T_a}$. In the case of $\mathbf{P_a}$, the field-effect mobility extrapolated to low carrier densities is almost three orders of magnitude higher than the lower estimate of the SCLC mobility. The deviation from the Mott-Gurney law hampers however a quantitative comparison between both mobilities. Two possible scenarios may nevertheless be outlined: (i) the discrepancy between SCLC and OFET data is only due to the injection barrier in SCLC devices. Since the carrier density dependence appears to be weak (Fig. 4), the actual $\mu_\perp$ value should then be close to $\mu_\parallel$. (ii) The out-of-plane mobility is significantly lower than the in-plane mobility (anisotropic charge transport) and contributes to the observed high $\mu_\parallel/\mu_\perp$ ratio. The microstructural investigations shown below will help us to elucidate this question.

The most surprising result is obtained on polymer $\mathbf{T_a}$. As shown in Fig. 4, the field-effect mobility exhibits a relatively pronounced charge carrier density dependence (high $E_0$), which hints towards a disordered material with isotropic transport, similar to $\mathbf{T_b}$ and $\mathbf{P_b}$. This conclusion is however in conflict with the measured out-of-plane mobility, which is almost one order of magnitude higher than $\mu_\parallel$. The latter result implies rather a high transport anisotropy, with a polymer microstructure that favors out-of-plane transport. In other words, the material appears to be characterized by a significant energy disorder but with a simultaneously high structural order (necessary to yield the observed transport anisotropy). Again, the microstructure analyses described below will help us to clarify this issue.

### 2.3 Polymer microstructure

**X-ray diffraction.** The 2D GIWAXS patterns measured for different polymers and geometries are presented in Fig. 5. $\mathbf{P_b}$ shows 2D GIWAXS patterns (see ESI†) similar to $\mathbf{T_b}$.

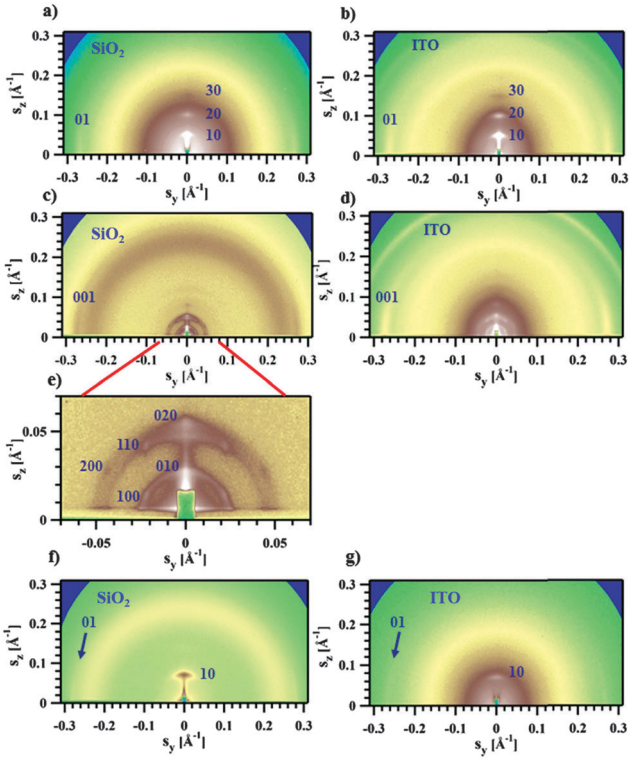


Fig. 5 GIWAXS patterns for OFET (left) or SCLC (right) devices for $\mathbf{P_a}$ [(a) and (b)], $\mathbf{T_a}$ [(c) and (d)] and $\mathbf{T_b}$ [(f) and (g)]. (e) is an enlarged small-angle region of image in (c). The incidence angle is 0.2°.

The GIWAXS experiments performed directly on the OFET and SCLC devices based on the $\mathbf{T_b}$ polymer reveal only one 10 peak in the out-of-plane direction (Fig. 5f and g). The equatorial 01 reflection corresponding to the regular π–π stacking at a distance of 3.76 Å is rather weak. These observations are in line with a disordered polymer presenting an isotropic charge transport. The same holds for $\mathbf{P_b}$.

The GIWAXS experiments performed on films of $\mathbf{P_a}$ in the transistor geometry (Fig. 5a) show that the X-ray peaks are located exclusively on the meridian and the equator. The reflections were indexed to a 2D unit cell, as shown in Fig. 5a. A set of meridional h0 reflections corresponds to a pronounced layer-like structure with an in-plane orientation of the polymer backbones. In addition, the pattern reveals a characteristic π–π stacking peak at a distance of 3.72 Å, which is located at the equator (denoted as 01 peak in Fig. 5a). Consequently, the chains are parallel to the film surface with an edge-on π–π stacking of the aromatic cores (as schematically depicted in Fig. 6a). A similar morphology was previously reported for P3HT.[26,27] The layer-like packing of the polymer chains is consistent with the high in-plane charge mobility measured for $\mathbf{P_a}$. Noteworthily, the GIWAXS pattern measured on a SCLC device looks similar (Fig. 5b), indicating that identical morphologies are observed for this polymer on two different substrates.

The active layer of $\mathbf{T_a}$ reveals well-oriented GIWAXS patterns (Fig. 5c–e), which are significantly different from the patterns

 

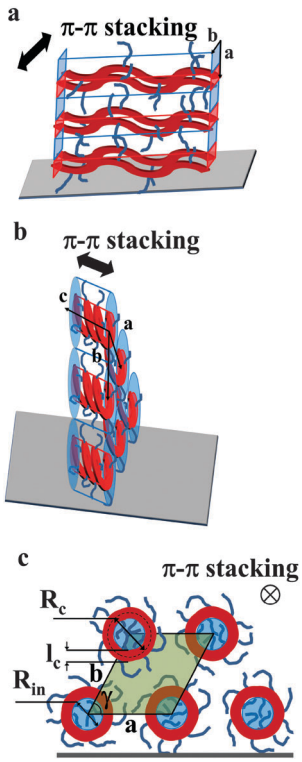


Fig. 6 Models schematically depicting the layer-like structure of thin films of $\mathbf{P_a}$ (a) and $\mathbf{T_a}$ (b). The polymer backbone is represented in red while the film surface is the gray parallelogram. (c) The view along the helical axis represents notations used in eqn (7) and (8). The inner part of the helices is colored in blue, the area of the pseudo-hexagonal unit cell external to the helices is colored in green (c).

discussed above. The appearance of the pattern is typical of columnar structures.[28] The analysis of the positions and intensities of the peaks in the small-angle region (Fig. 5e) makes it possible to assign the pattern to a monoclinic (pseudo-hexagonal) 2D columnar phase with the following parameters: $a$ = 53.0 Å, $b$ = 51.6 Å, $\gamma$ = 47.6°. Moreover, the equatorial peak at 3.57 Å indicates the development of an intra-columnar ordering. The calculated distance is close to the π–π stacking discussed above (see Fig. 5a). Therefore, it is likely that $\mathbf{T_a}$ does not form regular layer-like structures as $\mathbf{P_a}$, but forms instead a columnar structure with the in-plane columnar axis and the direction of π–π interactions parallel to the columnar axis. We speculate that for $\mathbf{T_a}$ the columns are formed from helices with the plane of the Th, TT and Bz rings normal to the helical axis. In this case, a dense packing of chemical units that constitute the neighboring helical pitches of the chain in the axial direction results in the formation of π–π interactions (Fig. 6b). Such intra-helical in-plane oriented π–π stacking can account for reasonable values of charge carrier mobility in the OFET geometry. It should be mentioned that experimental observations of a helical conformation for conjugated polymers are very scarce.[29] However, theoretical calculations of the conformational energy have been performed for several non-substituted semiconducting homopolymers (*e.g.*, polythiophene, polyfuran, and polypyrrol) showing that helical conformations of the conjugated backbone may be stable.[29] In this respect, our results probably constitute one of the rare experimental evidences of a helical backbone conformation for this class of polymers. It should be mentioned that most of the semicrystalline polymers in the crystalline state adopt a helical conformation of the backbone, and the often-encountered planar conformation is just a particular case of a helix although it is not called so. However, the exceptional feature of the helical conformation of the $\mathbf{T_a}$ backbone inferred from the X-ray diffraction data is its extremely large diameter as compared to the monomer size.

The observed qualitative difference between the conformation of $\mathbf{T_a}$ and that of the other polymers can be accounted for by the relatively low volume of grafted alkyl side groups per unit length of the polymer backbone. It is probable that the lower grafting density for $\mathbf{T_a}$ in the fully extended conformation is not sufficient to fill the inter-chain space when forming a lamellar arrangement. To verify this argument, we have estimated the thickness of the layers formed by the conjugated backbones and alkyl groups in a hypothetical layer-like morphology. The thicknesses of the layer populated by the side chains ($L_s$) and the main backbone ($L_c$) are proportional to the ratio of the corresponding volumes ($V_s$ and $V_c$, respectively):

$$\frac{L_s}{L_c} = \frac{V_s}{V_c} = \frac{M_{ws}\,\rho_c}{M_{wc}\,\rho_s} \qquad (6)$$

where $M_{ws}$, $M_{wc}$, $\rho_s$, and $\rho_c$ are molecular weights and densities of pure phases of alkanes and thiophenes, respectively. For $\mathbf{T_a}$, the ratio of volumes will be approximately one, consequently, the thickness of the alkyl and thiophene layers would be equal. Given the fact that the width of the backbone chain in the plane of thiophene rings ($l_c$) can be estimated as *ca.* 5 Å, the thickness of the alkyl layer should be identical. Taking into account the length of an extended dodecyl side chain (15Å), the tilt angle of the alkyl chain ($\varphi$), is equal to arcsin (5/15), or 18°. This unusually low angle leads us to the hypothesis of a "non-layered" morphology, which in our case will be based on a helical conformation adopted by the backbone.

Another argument for the helical model is that the shortest distance between grafting points along the $\mathbf{T_a}$ backbone is *ca.* 9.1 Å. For a layer-like structure, assuming full interdigitation of the side chains, the shortest inter-chain distance between alkyl groups along the backbone axis will be equal to 4.55 Å. This value significantly exceeds the distance between the alkyl chains both in a pure *n*-alkane phase (for example, for *n*-octane the distance is 4.0 Å) and in the regions formed by the side chains of a P3HT lattice (3.9 Å). Consequently, the relatively long distance between grafting points prevents the formation of a layer-like structure in $\mathbf{T_a}$. In contrast, the shortest distance between grafting points for $\mathbf{P_a}$ is *ca.* 5 Å, which is sufficient to form a dense alkyl layer. In the case of ethylhexyl substituted $\mathbf{T_b}$ and $\mathbf{P_b}$ the possibility of forming layer-like structures can be explained by a much lower density of the branched alkyl phase resulting in the formation of thicker side-chain layers.

The helical conformation in the $\mathbf{T_a}$ phase can compensate for the low density of the periphery. In addition, fine-tuning of

the alkyl density can be achieved by varying the number of side chains inside ($N_{in}$) and outside ($N_{out}$) of the helix (shown as a red circle in Fig. 6c). A simple calculation given below allows the estimation of $N_{in}$ and $N_{out}$ for the helical conformation of $\mathbf{T_a}$. The area of the helical chain cross-section $S_c$ (coloured in red in Fig. 6c) and the area of the inner part of the helix $S_{in}$ (coloured in blue) can be calculated from the number of monomers $n$ per turn of the helix and the backbone length of a monomer $L$:

$$S_c = nLl_c \quad (7)$$

$$S_{in} = \pi R_{in}^2 = \pi\left(R_c - \frac{l_c}{2}\right)^2 = \frac{1}{4\pi}(nL - \pi l_c)^2 \quad (8)$$

where $R_{in}$ and $R_c$ are the corresponding radii. The outer area $S_{out}$ (coloured in green) can be calculated as follows:

$$S_{out} = ab\,\sin\gamma - S_c - S_{in} \quad (9)$$

where $a$, $b$ and $\gamma$ are the parameters of the 2D unit cell.

Taking into account that the value of $n$ found from the macroscopic density is equal to six, and $L$ is approximately 17 Å, the values of $S_c$, $S_{in}$ and $S_{out}$, calculated from eqn (7)–(9) are 514, 607 and 898 Å$^2$, respectively. We consider that the packing density of the alkyl chains located inside and outside of the backbone is equal. In this case, the number of chains is proportional to the occupied volumes or surfaces. This allows us to find that $N_{in}$ = 5 and $N_{out}$ = 7. One can imagine that the alkyl density inside the helix can be lower because of the difficulty to efficiently pack in a narrow channel. If this is indeed the case, the difference between $N_{in}$ and $N_{out}$ will be even higher. The obtained value of $R_c$ (16.3 Å) is in fair agreement with the radius calculated for polythiophenes using density functional theory[30] (7.7 Å). It should be noted that the bigger radius of the helix in our case can be explained by the presence of bulky benzothiadiazole and thienothiophene groups in the backbone.

As far as charge transport is concerned, it is noteworthy that although the direction of the π–π stacking is along the columnar axes, the helical fragments of the chains can be relatively short. Non-regular loops of the helical backbones and ends of the chains, playing role of structural defects, can effectively overlap with the neighboring chains to provide good inter-chain charge transport. Also, because of a non-extended conformation of the alkyl groups, the distance between the main chains in the vertical direction of the columnar phase of $\mathbf{T_a}$ is shorter than that in the layer-like structure of $\mathbf{P_a}$. This can be the reason for a relatively high inter-chain mobility for $\mathbf{T_a}$ in the direction perpendicular to the substrate.

## 3. General discussion and conclusion

The GIWAXS data support and clarify the conclusions of the charge transport study. For the branched side-chain polymers ($\mathbf{T_b}$, $\mathbf{P_b}$) the measured highly disordered thin film morphology is in line with the high-energy disorder observed by the mobility measurements (Fig. 4). On the other hand, for $\mathbf{T_a}$ and $\mathbf{P_a}$, the GIWAXS structures reveal that charge transport is likely to be highly anisotropic. For $\mathbf{P_a}$ the pronounced lamellar morphology with in-plane π–π stacking interactions should favor in-plane transport and supports the inference that the orders of magnitude difference in OFET and SCLC mobilities is mostly due to anisotropic charge transport. The observed low energy disorder is then an expected outcome of the highly ordered microstructure. In addition, the more or less reproducible deviation from the Mott-Gurney law observed in $\mathbf{P_a}$-based SCLC devices might be a consequence of the presence of a dense layer of alkyl chains at the PEDOT:PSS/$\mathbf{P_a}$ interface that hinders charge injection.

The more intriguing charge transport observed in $\mathbf{T_a}$ thin films can also be clarified. The GIWAXS experiments show that $\mathbf{T_a}$ forms a rather unusual helical conformation of the conjugated backbone. Supposedly, the driving force for the helix formation in this structure with a relatively long distance between the chain grafting sites is the mismatch between the number of the side chains located inside and outside the helical scaffold. The regular turns of the helical backbone can account for the intra-chain π–π stacking in the direction parallel to the substrate, as revealed by a corresponding diffraction peak. Such structural organization comprising regular arrays of helices can account for a relatively high in-plane charge transport. In contrast, the shorter distance between neighboring helical polymer backbones in comparison to a perfectly layered structure, and the presence of conformational defects in $\mathbf{T_a}$ can explain why the value of $\mu_\perp$ is higher than $\mu_\parallel$. Interestingly, the higher interring torsion angles in such a helical conformation are expected to broaden the hopping site energy distribution.[5] The helicoidal microstructure should therefore enhance energy disorder (through a strong intra-molecular contribution) while leading to a relatively ordered molecular assembly. This behavior clarifies why the charge transport measurements lead simultaneously to a strong transport anisotropy ($\mu_\perp > \mu_\parallel$) and a high-energy disorder typical of amorphous (isotropic) polymers.

In summary, by combining in-plane as well as out-of-plane charge transport measurements and grazing incidence X-ray diffraction investigations on the same devices, we were able to show how minor changes along the polymer backbone of a conjugated low band-gap copolymer family can significantly impact the molecular assembly and lead to different charge transport properties. Branched side chains are found to increase structural disorder and lead to a broad DOS distribution and isotropic transport, while linear chains give rise to more ordered structures and strongly anisotropic transport. We further found strong experimental evidence that rather a rigid conjugated polymer can adopt a helicoidal structure, induced by a density mismatch. Furthermore, the correspondingly lower backbone planarity and larger interring torsion angles are responsible for a broader energy distribution of hopping sites. This observation confirms the assertion that in some cases, intra- rather than inter-molecular disorder can dominate energy disorder.[5]

 

# 4. Experimental section

### Space-charge-limited current devices

Hole-only SCLC devices were elaborated to investigate the out-of-plane mobility. The device structure was as follows: ITO/PEDOT:PSS/polymer/PEDOT:PSS/Al. Highly conductive poly(3,4-ethylenedioxythiophene):polystyrene-sulfonate (PEDOT:PSS) was used as the hole injection electrode. Indium tin oxide (ITO) coated glass with a sheet resistance of 20 Ω $sq^{-1}$ was used as a substrate. The ITO layer was cleaned sequentially by ultrasonic treatments in acetone, isopropyl alcohol and deionized water. After an additional 30 min exposure to ultra-violet generated ozone, a 40 nm thick PEDOT:PSS layer was spin-coated from an aqueous solution on top of the ITO layer and dried for 30 min at 120 °C under vacuum before being transferred to the nitrogen filled glove box. Dichlorobenzene polymer solutions of varying concentrations were prepared and stirred at 70 °C for 48h before spin-coating on top of PEDOT:PSS. The resulting polymer layer thickness ranged from approximately 200 nm (for the less dense solution) to up to 700 nm. A second 40 nm thick PEDOT:PSS layer was spin-coated on top of the polymer and dried under vacuum at 110 °C for 15 minutes. The devices were completed by thermal evaporation of 120 nm Al top electrode. The PEDOT:PSS layer was mechanically removed around the Al, limiting the device active area to the electrode surface (2 $mm^2$). Device elaboration and characterization were done at room temperature in a nitrogen-filled glove box. At least 4 devices have been analyzed for each polymer.

### Organic field-effect transistors

Bottom contact field-effect transistors were elaborated on commercial pre-patterned test structures. The lithographically defined source and drain contacts were composed of 30 nm thick gold on top of a 10 nm thick ITO layer and were deposited on top of an oxidized silicon wafer. The 230 nm thick silicon oxide was used as gate dielectric and the highly N-doped silicon substrate as a gate electrode. The transistor channel length ($L_c$) and width ($W$) were 20 μm and 10 mm long, respectively. The test structures were cleaned sequentially in acetone and isopropyl alcohol baths and in an ultra-violet ozone cleaner for 15 minutes. Hexamethyldisilazane (HMDS) was spin-coated under nitrogen ambient and annealed at 130 °C for 15 minutes. Finally, 4 mg $ml^{-1}$ anhydrous *ortho*-dichlorobenzene (*o*-DCB) polymer solutions were spin-coated to complete the OFET devices. The samples were left overnight under vacuum to remove residual solvent traces. Both the OFET elaboration and room temperature characterization were performed in a nitrogen-filled glove box. The temperature dependent measurements were performed in a He cryostat. In this case, exposure to air was limited to less than 5 minutes.

### Grazing-incidence wide angle X-ray scattering

Grazing-Incidence Wide-Angle X-ray Scattering (GIWAXS) experiments were performed on the BW4 beamline at HASYLAB (DORIS storage ring, DESY, Hamburg, Germany). Diffraction patterns were collected using a MAR CCD camera of 2048 × 2048 pixels with a resolution of 79.1 μm. The wavelength of 1.38 Å and a sample-to-detector distance of 160 mm were used in our experiments. The measurements were performed directly on OFET or SCLC devices with different incidence angles $\alpha_i$ = 0.2° and 0.3° with typical acquisition times of 120 s. The modulus of the scattering vector was calibrated using several diffraction orders of silver behenate.

# Acknowledgements

This work was supported by the European project Interreg IV Rhin-Solar (no C25). D.V.A. and D.A.I. acknowledge the Russian Ministry of Science and Education (grant no 14.604.21.0121). The authors are grateful to Dr Jan Perlich from the BW4 beamline at the Deutsches Elektronen-Synchrotron (DESY) for fruitful discussions and excellent technical support.

# Notes and references

1 C. Luo, A. K. K. Kyaw, L. A. Perez, S. Patel, M. Wang, B. Grimm, G. C. Bazan, E. J. Kramer and A. J. Heeger, *Nano Lett.*, 2014, **14**, 2764.
2 H. Sirringhaus, T. Sakanouey and J.-F. Chang, *Phys. Status Solidi B*, 2012, **9**, 1655.
3 A. Salleo, R. J. Kline, D. M. De Longchamp and M. L. Chabinyc, *Adv. Mater.*, 2010, **22**, 3812.
4 R. Noriega, J. Rivnay, K. Vandewal, F. P. V. Koch, N. Stingelin, P. Smith, M. F. Toney and A. Salleo, *Nat. Mater.*, 2013, **12**, 1038.
5 N. Vukmirovíc, *Phys. Chem. Chem. Phys.*, 2013, **15**, 3543.
6 D. Venkateshvaran, M. Nikolka, A. Sadhanala, V. Lemaur, M. Zelazny, M. Kepa, M. Hurhangee, A. J. Kronemeijer, V. Pecunia, I. Nasrallah, I. Romanov, K. Broch, I. McCulloch, D. Emin, Y. Olivier, J. Cornil, D. Beljonne and H. Sirringhaus, *Nature*, 2014, **515**, 384.
7 C. Tanase, P. W. M. P. Blom, D. M. de Leeuw and E. J. Meijer, *Phys. Status Solidi A*, 2004, **201**, 1236.
8 C. Tanase, E. J. Meijer, P. W. M. P. Blom and D. M. de Leeuw, *Phys. Rev. Lett.*, 2003, **91**, 216601.
9 C. Tanase, P. W. M. P. Blom and D. M. de Leeuw, *Phys. Rev. B: Condens. Matter Mater. Phys.*, 2004, **70**, 193202.
10 (*a*) L. Biniek, S. Fall, C. L. Chochos, D. V. Anokhin, D. A. Ivanov, N. Leclerc, P. Lévêque and T. Heiser, *Macromolecules*, 2010, **43**, 9779; (*b*) L. Biniek, S. Fall, C. L. Chochos, N. Leclerc, P. Lévêque and T. Heiser, *Org. Electron.*, 2012, **13**, 114.
11 S. Fall, L. Biniek, N. Leclerc, P. Lévêque and T. Heiser, *Appl. Phys. Lett.*, 2012, **101**, 123301.
12 M. A. Lampert and P. Mark, *Current Injection in Solids*, Academic Press, New York, USA, 1979.
13 C. Goh, R. Kline, M. D. McGehee, E. N. Kadnikova and J. M. J. Fréchet, *Appl. Phys. Lett.*, 2005, **86**, 122110.
14 G. Horowitz, D. Fichou, X. Peng and P. delannoy, *J. Phys.*, 1990, **51**, 1489.

15 G. A. H. Wetzelaer and P. W. M. Blom, *Phys. Rev. B: Condens. Matter Mater. Phys.*, 2014, **89**, 241201(R).
16 P. N. Murgatroyd, *J. Phys. D: Appl. Phys.*, 1970, **3**, 151.
17 R. Coehoorn and P. A. Bobbert, *Phys. Status Solidi A*, 2012, **209**, 2354.
18 G. Horowitz, P. Lang, M. Mottaghi and H. Aubin, *Adv. Funct. Mater.*, 2004, **14**, 1069.
19 J. O. Oelerich, D. Huemmer and S. D. Baranovskii, *Phys. Rev. Lett.*, 2012, **108**, 226403.
20 C. Tanase, E. J. Meijer, P. W. M. Blom and D. M. de Leeuw, *Org. Electron.*, 2003, **4**, 33.
21 M. C. J. M. Vissenberg and M. Matters, *Phys. Rev. B: Condens. Matter Mater. Phys.*, 1998, **57**, 12964.
22 A. V. Nenashev, J. O. Oelerich and S. D. Baranovskii, *J. Phys.: Condens. Matter*, 2015, **27**, 093201.
23 Z. Chen, M. Bird, V. Lemaur, G. Radtke, J. Cornil, M. Heeney, I. McCulloch and H. Sirringhaus, *Phys. Rev. B: Condens. Matter Mater. Phys.*, 2011, **84**, 115211.
24 S. D. Baranovskii, O. Rubel, F. Jansson and R. Österbacka, in *Organic Electronics*, ed. G. Meller and T. Grasser, Springer, Heidelberg, Germany, 2010, ch. 3.
25 H. Bässler, in *Semiconducting polymers*, ed. G. Hadziioannou and P. F. van Hutten, Wiley, New York, 2000.
26 (*a*) M. Brinkmann and J. C. Wittmann, *Adv. Mater.*, 2006, **18**, 860; (*b*) R. J. Kline, M. D. McGehee, E. N. Kadnikova, J. Liu, J. M. J. Fréchet and M. F. Toney, *Macromolecules*, 2005, **38**, 3312.
27 S. Ko, D. Hwan Kim, A. L. Ayzner, S. C. B. Mannsfeld, E. Verploegen, A. M. Nardes, N. Kopidakis, M. F. Toney and Z. Bao, *Chem. Mater.*, 2015, **27**, 1223.
28 (*a*) R. I. Gearba, A. I. Bondar, M. Lehmann, B. Goderis, W. Bras, M. H. J. Koch and D. I. Ivanov, *Adv. Mater.*, 2005, **17**, 671; (*b*) C. L. Wang, W. B. Zhang, C. H. Hsu, H. J. Sun, R. M. Van Horn, Y. Tu, D. V. Anokhin, D. A. Ivanov and S. Z. D. Cheng, *Soft Matter*, 2011, **7**, 6135; (*c*) R. I. Gearba, D. V. Anokhin, A. I. Bondar, W. Bras, M. Lehmann and D. A. Ivanov, *Adv. Mater.*, 2007, **19**, 815.
29 M. Brinkmann, N. Charoenthai, R. Traiphol, P. Piyakulawat, J. Wlosnewski and U. Asawapirom, *Macromolecules*, 2009, **42**, 8298.
30 J. D. Ripoll, A. Serna, D. Guerra and A. Restrepo, *J. Phys. Chem. A*, 2010, **114**, 10917.

 